Delft University of Technology

Thermo-Mechanical EM Models for Broadband Cryogenic VNA Calibration Including Numerical Uncertainties Down to 4.2 K

Shokrolahzade, E.; Mubarak, F. A.; Wiedmayer, J.; Martino, C. De; Oberto, L.; Sebastiano, F.; Spirito, M.

DOI
10.1109/TMTT.2025.3584196

Publication date
2025

Document Version
Final published version

Published in
IEEE Transactions on Microwave Theory and Techniques

Citation (APA)
Shokrolahzade, E., Mubarak, F. A., Wiedmayer, J., Martino, C. D., Oberto, L., Sebastiano, F., & Spirito, M. (2025). Thermo-Mechanical EM Models for Broadband Cryogenic VNA Calibration Including Numerical Uncertainties Down to 4.2 K. *IEEE Transactions on Microwave Theory and Techniques*, *73*(11), 9058-9069. https://doi.org/10.1109/TMTT.2025.3584196

Important note
To cite this publication, please use the final published version (if applicable).
Please check the document version above.

Copyright
Other than for strictly personal use, it is not permitted to download, forward or distribute the text or part of it, without the consent of the author(s) and/or copyright holder(s), unless the work is under an open content license such as Creative Commons.

Takedown policy
Please contact us and provide details if you believe this document breaches copyrights.
We will remove access to the work immediately and investigate your claim.

This work is downloaded from Delft University of Technology.
For technical reasons the number of authors shown on this cover page is limited to a maximum of 10.

Green Open Access added to TU Delft Institutional Repository
as part of the Taverne amendment.

More information about this copyright law amendment
can be found at https://www.openaccess.nl.

Otherwise as indicated in the copyright section:
the publisher is the copyright holder of this work and the
author uses the Dutch legislation to make this work public.

Thermo-Mechanical EM Models for Broadband Cryogenic VNA Calibration Including Numerical Uncertainties Down to 4.2 K

E. Shokrolahzade, *Graduate Student Member, IEEE*, F. A. Mubarak, *Senior Member, IEEE*, J. Wiedmayer, C. De Martino, *Member, IEEE*, L. Oberto, F. Sebastiano, *Senior Member, IEEE*, and M. Spirito, *Member, IEEE*

***Abstract*—Increasing demand for cryogenic electronics aimed at quantum sensors and computing technologies asks for accurate and quantifiable calibration methods and techniques. In this work, we present a structured approach to generate the nominal RF responses of standard artifacts, enabling wideband vector network analyzer (VNA) calibration algorithms, i.e., short, open, load, and reciprocal (SOLR), at cryogenic temperatures. Moreover, we present an EM simulation strategy to generate the perturbations in the artifacts' responses based on mechanical fabrication tolerances and calculate an equivalent RF response uncertainty. Both the nominal and perturbed standard responses are computed at (user defined) cryogenic temperatures, by combining thermo-mechanical responses with the electromagnetic solver. A circuit simulator-based measurement model (MM) is used to compute the uncertainties of the cryogenic setups used in this work. Error contributions arising from the propagation of VNA noise, switch nonidealities, calibration artifacts uncertainties, temperature fluctuations, and temperature gradient over the interconnects are included in the MM. For validation, measured results of a coaxial air transmission line at 77 K and 4.2 K are presented and compared with 3-D EM simulation predictions. Finally, the measurement uncertainties are detailed in a budget analysis describing the individual contributions.**

***Index Terms*—Cryogenic measurements, low temperature measurement, microwave calibration, *S*-parameters, uncertainty analysis, vector network analyzer (VNA).**

Received 22 March 2025; revised 21 May 2025 and 21 June 2025; accepted 25 June 2025. Date of publication 10 July 2025; date of current version 26 November 2025. This work was supported in part by EuropeanSuperQuant and in part by the SuperQuant through the European Metrology Programme for Innovation and Research (EMPIR) Program Co-Financed by the Participating States and European Union's Horizon 2020 Research and Innovation Program under Project 20FUN07. *(Corresponding author: E. Shokrolahzade.)*

E. Shokrolahzade, C. De Martino, and M. Spirito are with the Electronic Circuits and Architectures Group, Delft University of Technology, 2628 CD Delft, The Netherlands (e-mail: e.shokrolahzade@tudelft.nl; c.demartino-1@tudelft.nl; m.spirito@tudelft.nl).

F. A. Mubarak is with the VSL National Metrology Institute of the Netherlands, 2629 JA Delft, The Netherlands (e-mail: FMubarak@vsl.nl).

J. Wiedmayer is with XMA Corporation, Manchester, NH 03103 USA (e-mail: JWiedmayer@xmacorp.com).

L. Oberto is with the Istituto Nazionale di Ricerca Metrologica, 10135 Turin, Italy (e-mail: l.oberto@inrim.it).

F. Sebastiano is with the Department of Quantum and Computer Engineering, Delft University of Technology, 2628 CJ Delft, The Netherlands, and also with QuTech, 2628 CJ Delft, The Netherlands (e-mail: f.sebastiano@tudelft.nl).

Digital Object Identifier 10.1109/TMTT.2025.3584196

I. Introduction

Cryogenic RF circuits and systems are used in various cutting-edge technologies, covering fields from quantum computing to astrophysical observations and particle physics [1], [2], [3], [4].

Accurate characterization and modeling of the components, both active and passive, used to realize the circuits targeted for these applications, play a crucial role in the further development and uptake of these technologies [5], [6], [7], [8].

High-frequency device characterization sets its accuracy by precise removal of the systematic errors introduced by the measurement setup, in the calibration process. To acquire and remove systematic errors in *S*-parameter measurements, multiple artifacts with known RF responses, either full or partial, depending on the calibration algorithm, are measured in the process [9]. In the cryogenic environment, no physical replacement of the calibration artifacts is possible without breaking the cold state. For this reason, the entire calibration process can only be carried out over multiple cooling cycles or by using cryo-compatible switches in the calibration path, as was introduced in [10]. The latter has become the preferred method [11], [12] thanks to the reduced impact of temporal-related uncertainties in the calibration procedure, such as drift and setup alterations. Moreover, moving to a single cooling step minimizes the otherwise extremely long experiment duration, making these setups more practical in the R&D environment. In the last decade, different approaches have been employed to derive the cryogenic calibration standard definitions, from the direct usage of the measured ambient temperature responses [13], to employing air transmission lines with longitudinal single-dimensional scaling in a cryogenic TRL procedure [14], to the generation of cryogenic standard definitions transferring the cryogenic TRL calibration (with its bandwidth limitation) onto the lumped standards (i.e., short, open, and load) placed in the low temperature cryostat [12].

While the recent scientific literature has highlighted the improvement in fully calibrated test-benches with a single cooling cycle (summarized in Table I), there is still a lack of cryogenic broadband calibration standards, defined from the MHz range to the setup upper limit, to enable accurate measurements for device model extraction and verification.

Moreover, there is a current lack of a complete uncertainty budget calculation for cryogenic measurement, including both

0018-9480 © 2025 IEEE. All rights reserved, including rights for text and data mining, and training of artificial intelligence and similar technologies. Personal use is permitted, but republication/redistribution requires IEEE permission.
See https://www.ieee.org/publications/rights/index.html for more information.

Authorized licensed use limited to: TU Delft Library. Downloaded on December 08,2025 at 08:18:55 UTC from IEEE Xplore. Restrictions apply.

TABLE I
COMPARISON WITH STATE-OF-THE-ART PAPERS WITH CONNECTORIZED SETUPS

	This work	Arakawa et.al.[15]	Stanley et.al.[11]	Stanley et.al.[12]	Simbierowicz et.al.[13]	Shin et.al.[16]	Wang et.al.[17]
Calibration Algorithm	SOLR[18]	SOLT	mTRL	SOLR	SOL	mTRL	SOL
Standard Definition	EM(CST) Full structure	RT ECal	EM(CST): Z_0	TRL at 3 K	RT ECal	Z_0 via estimated shrinkage	RT Database
Standard Temp.	77 K, 4.2 K	RT	<20 mK	3 K	RT	30 mK	RT
Measurement Temperature	77 K , 4.2 K	4-300 K	<25 mK	3 K	30 mK	30 mK	15 mK
Frequency Range	0.05 – 20 GHz	2 MHz-26.5 GHz	1 – 10 GHz	0.5 – 18 GHz	0.01 – 18 GHz	0.5 – 18 GHz	4 – 8 GHz
Uncertainty Analysis	Monte Carlo	NA	NA	NA	$\sqrt{\sigma^2_{S_{11},ECAL\,(RT)} + \sigma^2_{S_{11},Switch\ var}}$	NA	NA
Verification	Air Transmission Line S-Parameters	Flush Thru	NA	NA	NA	Air Transmission Line Z_0 compared	NA

setup uncertainties and cryogenic standard uncertainties, with broadband calibration standards. Such an uncertainty budget would allow for isolating the sources of error that largely contribute to the overall uncertainty, with the general goal of improving the metrology quality of cryogenic measurements. In addition, such uncertainty budget calculation/estimation could allow isolating measurement setup uncertainty from the device under test (DUT) process variation. This is a crucial step to improve the modeling and understanding of technologies used outside their classical operation ranges, as in [19].

In this contribution, we present a simulation-assisted approach to enable true broadband cryogenic calibration capability based on the following two-step procedure.

1) Usage of 3-D thermo-mechanical simulation of devices employed in the calibration and verification process, in which the mechanical contraction of the artifacts, caused by temperature change, is applied at different temperatures (i.e., 77 K and 4.2 K).
2) Full-wave EM simulation of the modified structures to acquire the nominal responses of the artifacts at the user-defined temperature.

The proposed approach is independent of setup limitations, as it allows for generating "true" broadband cryogenic responses of the calibration artifacts. Thus, setup imperfections, such as switch asymmetries and frequency limitations, are not transferred to the standard definitions. To include standard residuals, the proposed approach considers device mechanical tolerances (i.e., fabrication-centric) as opposed to the more common definition based on measurement uncertainties (i.e., laboratory-centric). In the conventional approach, only available at room temperature (RT) or where a primary standard is present, the uncertainties of the measurement setup used to extract the artifact response, are propagated to the measured data, defining the uncertainty for the specific DUT. In the approach proposed in this work, the fabrication tolerances are mapped as an uncertainty bound and scaled to the defined temperature, compounding the "family" of responses for that device/fabrication process, detailed in Section II.

Finally, this contribution presents, for the first time to the best of the author's knowledge, a complete uncertainty budget analysis, based on a circuit simulator measurement model (MM) [20], of the different cryogenic setups employed in this work.

This article is structured as follows: Section II presents details on the EM modeling of devices, Section III describes the cryogenic modeling of device nominal and perturbed responses. The proposed circuit simulator-based MM is described in Section IV. Section V details the modeling approach to account for cable and interconnect temperature gradients and fluctuations, and Section VI describes the inclusion of switch nonidealities. Finally, in Section VII, measurement setups and results for calibration and validation at 77 K and 4.2 K are shown and discussed in Section VIII.

II. EM-BASED STANDARDS RESPONSE

The work carried out in this contribution is based on cryogenic terminations [21], [22], [23] fabricated by XMA corporation with sub miniature version A (SMA) connectors for the vector network analyzer (VNA) calibrations and a Wiltron 75 mm 19SA50 precision coaxial air transmission line utilized as a verification device. For the full-wave electromagnetic EM simulations, CST Studio Suite software from Dassault Syst'emes is used [24].

A. EM Model Generation

The 3-D models implemented in the full-wave (EM) simulations are based on the mechanical models used in the fabrication process. The dimensions are specified at RT, assumed to be 293.15 K in this study, and include the RT electrical properties of the materials, such as conductivity, dielectric constant, and loss tangent.

The modeling (i.e., 3-D representation) of the metallic parts of the devices includes the following simplifications.

1) The stratification of the thin gold compound plating on top of the copper beryllium base is removed from the models. A uniform material employing the electrical properties of gold and thermo-mechanical properties of copper beryllium is instead used. It is worth noting that

Authorized licensed use limited to: TU Delft Library. Downloaded on December 08,2025 at 08:18:55 UTC from IEEE Xplore. Restrictions apply.

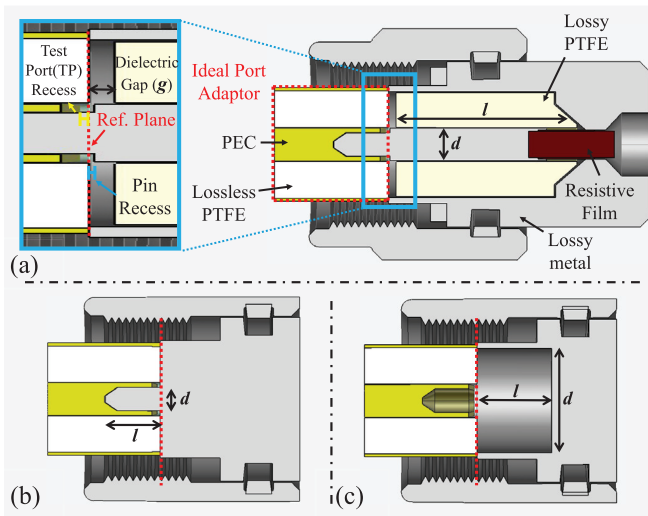

Fig. 1. Cross section view of the mechanical model of (a) SMA load standard. (b) SMA short standard. (c) SMA open standard with the lossless adaptor employed in the full-wave 3-D EM simulations.

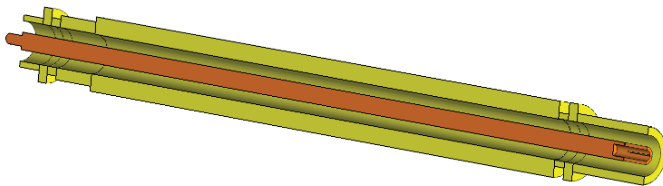

Fig. 2. Cross section view of CST model of the 75 mm air transmission line (pin color altered for visibility).

the loss contribution of the base material is only relevant at lower frequencies below the skin depth of the layer, where the conductive losses are already extremely low.

2) No surface roughness is considered in the models.

The simplification choices described above allow for optimizing the meshing process and minimizing computation time.

To derive the response of the calibration components (i.e., short, open, and load) shown in Fig. 1, an ideal port adaptor is used to interface the CST waveguide port to the pin/socket connector. This adaptor is required as the waveguide port in the simulation software needs an even plane to excite the proper (Quasi-TEM) EM mode. The geometry and dimensions of the adaptor are based on those of the coaxial test-port used in the experiments (SMA). The adaptor is composed of a lossless dielectric with the same permittivity as that used in the component and perfect electrical conductor (PEC) parts, as shown in Fig. 1. The response of this port adaptor is removed by the CST de-embedding process as a homogeneous transmission line, producing the same results as obtained by a conventional ABCD matrix de-embedding [25]. The recess on the adaptor corresponds to the recess of the measurement test port [see Fig. 1(a), test port recess] and increases the model to hardware correlation. This is necessary as the open standard structure does not have a pin, and this recess will impact its RF response.

The nominal response of the transmission line validation device, employed in Section VII, is acquired from a 3-D model, shown in Fig. 2, with the same simplifications of metallic parts.

B. Process Variation at RT

The EM simulations provide the nominal responses for the components, which allows us to numerically derive the knowledge to carry out the deterministic part of the device responses (similar to [26] and [27]). As previously mentioned, the RT uncertainty of a specific device, is obtained by propagating the combination of calibration residuals (obtained from the primary calibration) and the setup uncertainties through the calibration equations [28], [29], [30]. In a cryogenic environment, the same approach is not possible due to the lack of a primary calibration. Therefore, in this contribution, we derive the residuals of the device responses used in the calibration process from parametric EM simulations. This is realized by incorporating the device's mechanical and electrical tolerances (i.e., machining and sample variation) in the EM simulations, thus generating a "family" of responses for the same device (i.e., short, open, and load).

The models for the devices used in this study were parameterized, using four parameters for the load, three for the short, and two for the open standard. The parameters are labeled in Fig. 1, while the tolerances employed in the parametric EM simulations, are mapped in Table II. Note, the load internal dielectric length tolerance has only a positive occurrence per assessments of the manufacturer. The Bottom plane offset in the short standard parameters is the nonideal gap between the ideal adaptor and reflecting plate of the short standard (adjacent to the reference plane), causing delays in phase.

Fig. 3 presents the RT nominal response of the short artifact with the uncertainty bound extracted from the parametric simulations, providing a 3σ coverage(99.7% confidence interval) of the total variations. Similar responses are also obtained for the load and open standards, and are not presented in graphical form for space considerations. This σ is calculated assuming a Gaussian distribution of the responses according to type B uncertainty response guidelines [31]. Given the high number of mesh cells, a reduction to only the combinations of maximum, minimum, and nominal of each perturbation parameter was used, resulting in 54 loads, 27 shorts, and nine open simulations to be used for the computation of the artifacts' residual uncertainty.

It is important to mention that the model uncertainty for the load is expanded in the area underlying the nominal value to zero to account for the higher possible fabrication variation of this device.

To provide a first-level validation of the EM derived responses with their estimated uncertainties, the parametric simulations are compared with traceable measurements. Four instances of each device were measured in RT at the Dutch metrology institute VSL, and they are depicted in Fig. 4, each with separate measurement uncertainty (dark blue). The combined load uncertainty is considered to expand over the limited number of samples available (light blue region with black lines). The comparison between the numerical model responses and experimental data, both with their uncertainty bounds, is given in Fig. 4.

As can be seen by the various plots in Fig. 4(a), good agreement is found between the model, the measurements, and their respective bounds. It is worth noting that the numerical

Authorized licensed use limited to: TU Delft Library. Downloaded on December 08,2025 at 08:18:55 UTC from IEEE Xplore. Restrictions apply.

TABLE II
MODEL MANUFACTURING PARAMETERS USED FOR PERTURBATION

	Parameter Description	Symbol	Temp (K)	Nominal value inch (μm)	Max Tolerance inch (μm)
Load	PTFE cylinder length	l	293.15 K	0.28 (7112)	+4E-3 (101.60)
			77 K	0.273 (6930)	+3.90E-3 (99.06)
			4.2 K	0.269 (6830)	+3.85E-3 (97.79)
	PTFE ε_r	-	293.15 K-4.2 K	2.1	±1E-2
	Dielectric gap	g	293.15 K	8.5E-3 (215.9)	±1E-3 (25.4)
			77 K	1.161E-2 (294.9)	9.9E-4 (25.15)
			4.2 K	1.335E-2 (339.1)	9.88E-4 (25.09)
	Center pin outer diameter	d	293.15 K	0.05 (1270.0)	±2E-3 (50.8)
			77 K	0.04985 (1266.2)	1.9994E-3 (50.784)
			4.2 K	0.04984 (1265.9)	1.99936E-3 (50.783)
Short	Center pin outer diameter	d	293.15 K	0.036 (914.4)	±2E-3 (50.8)
			77 K	0.03589 (911.6)	1.994E-3 (50.6)
			4.2 K	0.03588 (911.3)	1.93E-3 (49.0)
	Bottom plane offset	-		0 (0)	±1E-3 (25.4)
	Center pin length	l	293.15 K	0.085 (2159)	±1E-3 (25.4)
			77 K	0.0836 (2123)	9.97E-4 (25.32)
			4.2 K	0.08358 (2122.9)	9.965E-4 (25.31)
Open	Inside diameter of chamber	d	293.15 K	0.162 (4114.8)	±2E-3 (50.8)
			77 K	0.16151 (4102.4)	1.994E-3 (50.65)
			4.2 K	0.16143 (4100.3)	1.993E-3 (50.62)
	bottom plane Offset	l	293.15 K	0.115 (2921)	±1E-3 (25.4)
			77 K	0.11465 (2912.1)	9.97E-4 (25.32)
			4.2 K	0.11459 (2910.6)	9.965E-4 (25.31)

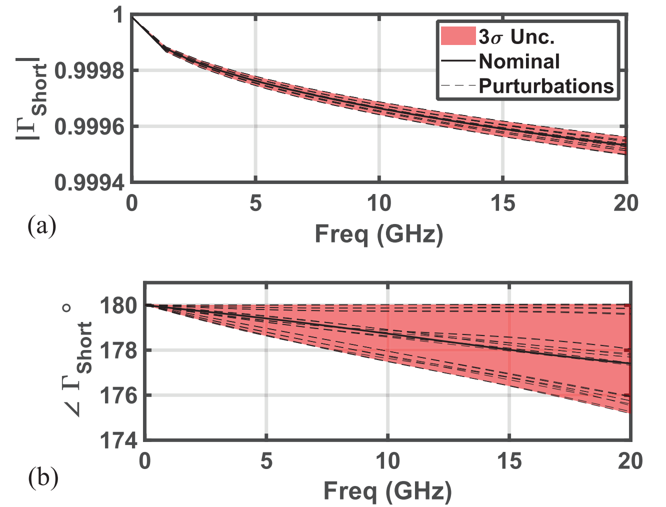

Fig. 3. Numerical RT response of the SMA short used in this work, including the nominal response and the 3σ uncertainty bound calculated from the parametric EM response using the perturbation values described in Table II. (a) Shows $|\Gamma_{\text{Short}}|$ and (b) shows $\angle\Gamma_{\text{Short}}$.

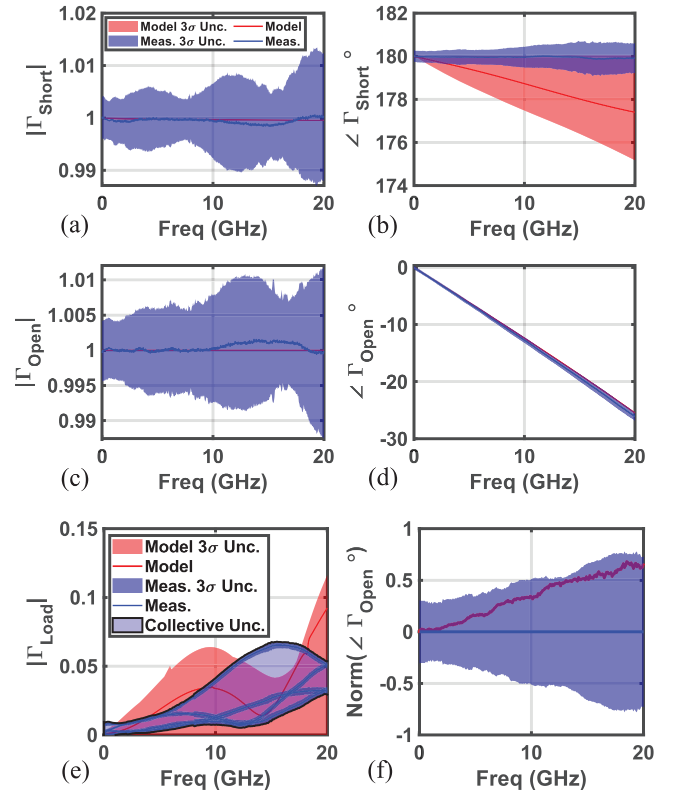

Fig. 4. Comparison of EM simulations responses of standards at RT with process fabrication uncertainty bounds, versus measured responses of the same standards, performed at VSL, (a) shows a comparison for $|\Gamma_{\text{Short}}|$, (b) for $\angle\Gamma_{\text{Short}}$, (c) for $|\Gamma_{\text{Open}}|$, (d) for $\angle\Gamma_{\text{Open}}$, (e) for $|\Gamma_{\text{Load}}|$, and (f) for $\text{Norm}(\angle\Gamma_{\text{Open}}) = \angle\Gamma_{\text{Open}} - \angle\Gamma_{\text{Open meas}}$.

bounds on the magnitude component of the low-loss reflect standards are smaller than the experimental ones, since no contact resistance is present in the EM simulation. Contrary, a larger bound for the phase components in the EM generated bounds is shown, which is a direct result of including all the process fabrication tolerances. For the load artifacts [Fig. 4(e)], multiple measurement lines are shown with a shared uncertainty region (light blue) to highlight the larger inter-component variation of this device, due to the presence of a resistive layer and a dielectric core. To better illustrate the difference between the measured data and the model response, Fig. 4(f) presents the normalized $\angle\Gamma_{\text{Open}}$, which is calculated using the expression, $\text{Norm}(\angle\Gamma) = \angle\Gamma - \angle\Gamma_{\text{Ref}}$, for both the uncertainty bound and the nominal response.

III. Thermo-Mechanical Flow for Cryogenic Response

To generate the response of the devices used in the calibration process at different temperatures (i.e., 77 K and 4.2 K), the approach proposed in this work is to combine the artifact thermo-mechanical variation due to the temperature

Authorized licensed use limited to: TU Delft Library. Downloaded on December 08,2025 at 08:18:55 UTC from IEEE Xplore. Restrictions apply.

TABLE III
CRYOGENIC MATERIAL PROPERTIES

	Parameter description	Temp.	Value
Gold	Conductivity	293.15 K	4.29 E+7 S/m
		77 K	5.357 E+9 S/m
		4.2 K	6.84 E+9 S/m
Copper Beryllium	Young's module	293.15-4.2 K	127.5 GPa
	Poisson's ratio	293.15-4.2 K	0.30
	Specific heat	293.15-4.2 K	420 J/K/kg
	293.15-4.2 K	117.5 W/K/kg	Thermal conductivity
	Thermal expansion coefficient	293.15 K	Unused 17E-6 /K
		293.15- 77 K	13.6 µ/K (mean value)
		293.15-4.2 K	10.8 µ/K (mean value)
PTFE	Electrical permittivity	293.15-4.2 K	2.1
	Tan δ	293.15 K	2 E-4
		77 K	4 E-6
		4.2 K	1 E-6
	Young's module	293.15-4.2 K	0.5 GPa
	Poisson's ratio	293.15-4.2 K	0.4
	Specific heat	293.15-4.2 K	1000 J/K/kg
	Thermal conductivity	293.15-4.2 K	0.2 W/K/kg
	Thermal expansion coefficient	293.15 K	Unused
		293.15- 77 K	140 µ/K (mean value)
		293.15-4.2 K	71.8 µ/K (mean value)

geometry. These EM simulations also incorporate the changes in the electrical properties of the composing materials at the defined temperature. Both the coefficient of thermal expansion (CTE) of the materials as well as their electrical properties are acquired from the literature [32], [33], [34], and [35] as summarized in Table III. Since none of the components used in this study are hermetic, the background materials in the simulation environments are replaced with the cooling liquids for the cryogenic models (i.e., liquid nitrogen for the 77 K and liquid helium for the 4.2 K).

The thermo-mechanical simulation assumes that the devices are fully thermalized, the materials are homogenous and isotropic, and that their spatial orientation with respect to gravity direction has negligible effects on the contraction of the devices. Thus, the shrinkage effect occurs uniformly for every cardinal axis, see Fig. 5. For this reason, we extract from the compressed 3-D model, a scaling factor for each material

TABLE IV
CST SIMULATOR SETTINGS

Parameter		Value
FEM	Boundaries	Open and Open add space (Port-side)
	Solver accuracy	1E-6
	Excitation	Waveguide ports (Single mode)
THs	Starting Temperature	293.15 K
	Accuracy	1E-6
	Excitation	Temperature source
	Boundaries	Open add space
ST	Accuracy	1E-4
	Excitation	Thermal field import
	Mesh type	Tetrahedral
Symmetry		2-planes
Background		Normal (custom ε_r)
Solver order		2nd order

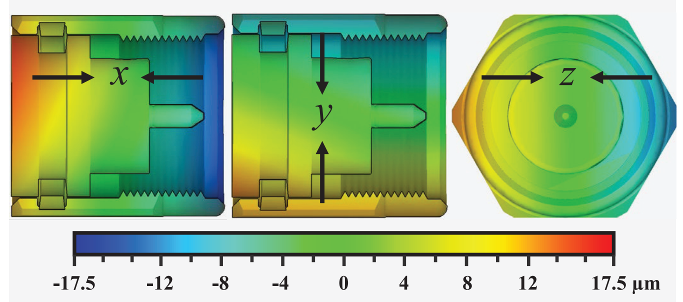

Fig. 5. Thermally induced mechanical displacement in longitude and transverse axis with respect to device center shown for a short device at 4.2 K.

used in the artifact along the three cardinal axis and apply them to the RT model and its mechanical perturbations. In the cryogenic models, the metallic sections of the components are scaled with 1:0.9970 and 1:0.9968 ratios for 77 K and 4.2 K, respectively, and with 1:0.9860 and 1:0.9810 for Teflon. The model dimensions for all temperatures are listed in Table II. This approach avoids long simulation times and errors due to the differences between thermal, mechanical, and EM mesh grids.

To avoid the manual task, the perturbation simulations are automated using a MATLAB [36] script controlling the CST simulation environment. The following flow is then implemented by the script.

1) Opens the device simulation file and updates the parameters.
2) Runs the simulation for every perturbation and saves the results.
3) Repeats the procedure of 1) and 2) for all (the user selected) temperatures.

For EM simulations, the CST frequency domain solver (FEM) was utilized and for the thermo-mechanical simulations, the CST steady state thermal solver (THs) and the mechanical solver (ST) were used. The settings used in the simulations are listed in Table IV.

Authorized licensed use limited to: TU Delft Library. Downloaded on December 08,2025 at 08:18:55 UTC from IEEE Xplore. Restrictions apply.

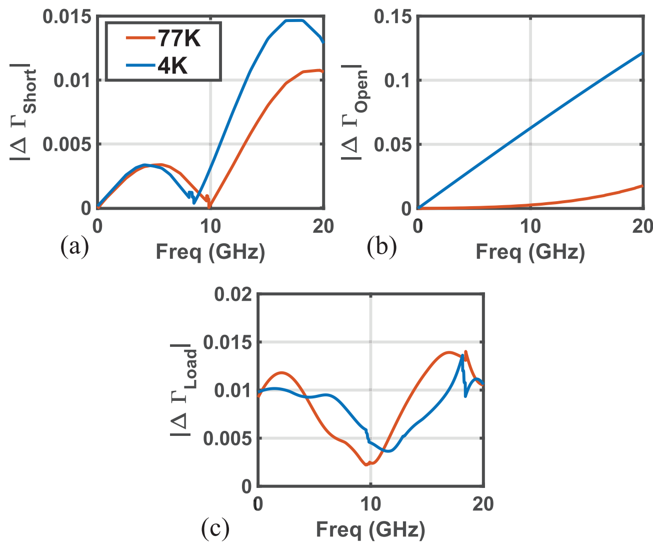

Fig. 6. Standards responses comparison over different temperatures: (a) short, (b) open, and (c) load.

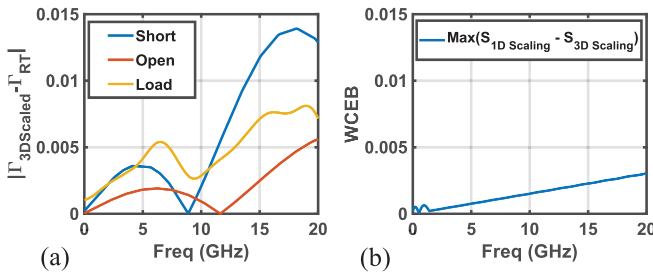

Fig. 7. (a) Complex vector difference ($|\Gamma_{3\text{-D scaled}} - \Gamma_{\text{Notscaled}}|$) of standard responses of 4.2 K standards with 3-D scaled models versus not scaled models. (b) WCEB of an air transmission line at 4.2 K, 1-D scaled with respect to the 3-D scaled case as reference.

In Fig. 6, the absolute difference between the room-temperature and the cryogenic reflection coefficient of the devices versus frequency are shown for each standard, computed using (1). It provides quantitative information on the change of the one-port standard when changing temperatures

$$|\Delta\Gamma| = |\Gamma_{\text{Cryo}} - \Gamma_{\text{RT}}|. \quad (1)$$

To quantify the impact of the 3-D scaling on the responses of the standards used in the calibration process, Fig. 7(a) presents the complex difference at 4.2 K between the case where no mechanical scaling is considered (i.e., only material response shift) and the full 3-D scaling with change in material properties (i.e., the proposed approach). As can be seen by the values of the vector difference in Fig. 7(a), the proper scaling is required when an accurate calibration is targeted, considering that an error below 0.01 (linear) in Γ is often the accuracy level required by the calibration process.

Likewise, as shown in Fig. 6, the $|\Delta\Gamma|$ of standards with respect to RT is higher than the 0.01 accuracy limit, indicating the need to use cryogenic standard responses.

It is important to mention that when considering traveling standards, i.e., coaxial air transmission lines for the calibration process/validation, as in [16] and [37], the often employed 1-D scaling provides sufficient accuracy. Using the worst case error bound (WCEB) metric [38], shown in (2), the difference between 1-D to 3-D scaling, see Fig. 7(b), is negligible

$$\text{WCEB} = \max \left|S_{ij} - S'_{ij}\right| \quad (2)$$

where S is the scattering matrix (1-D-scaled transmission line) and S' is the reference scattering matrix (3-D-scaled transmission line), and $i, j \in [1, 2]$.

The two temperatures, 77 K and 4.2 K, used in this study for the models are the boiling points of liquid nitrogen (LN_2) and helium (He), respectively, and are used in the experiments presented in Section VII.

IV. Numerical MM for Uncertainty Estimation

To increase confidence in cryogenic RF measurements and to allow inter-laboratory comparisons, this work proposes the usage of a numerical MM to evaluate the measurement uncertainties [20]. The MM is realized in two parts.

1) Part one is a schematic model of the measurement setup, using a circuit simulator environment to allow a strong correlation between the model and the hardware implementation. The proposed implementation was realized in Keysight Advance Design System (ADS) [39]. The simplified sketch of the ADS schematic environment is shown in Fig. 8.
2) Part two is a MATLAB script that controls the ADS environment, conveying the address of data files, running (Monte Carlo) simulations, gathering results, adding VNA noise, and applying calibration equations.

The ADS schematic is composed of RF components from the simulator library (i.e., the source, couplers, and so on), measurement-based data (i.e., the purple blocks in Fig. 8), which allows the nominal response of the simulation to match the systematic errors of the laboratory test setup closely, and a set of *S*-parameter blocks where the EM simulated response of the components can be loaded (i.e., the calibration and verification artifacts).

To add calibration device uncertainties and the effects of cable temperature fluctuation uncertainties to the MM, we employ Monte Carlo simulations. These effects are conveyed through changing the data blocks used by the ADS schematic.

Embedding a combination of synthetic and measurement data in the MM allows for proper propagation of the uncertainties to the device level by applying realistic systematic errors and the calibration equations on the results.

It is important to note that the proposed MM does not aim to replace uncertainty calculating software like METAS VNA-Tools [40] or NIST Microwave Uncertainty Framework [41], but aims to provide a tool with strong hardware correlation that allows to compare and optimize complex measurement architectures by providing numerical uncertainty data (prior) to the measurement experiments.

A. VNA Noise Inclusion

In this work, the VNA noise is added, in the MATLAB script, to the incident and reflected waves from the ADS simulation. The noise of the waves is calculated according

Authorized licensed use limited to: TU Delft Library. Downloaded on December 08,2025 at 08:18:55 UTC from IEEE Xplore. Restrictions apply.

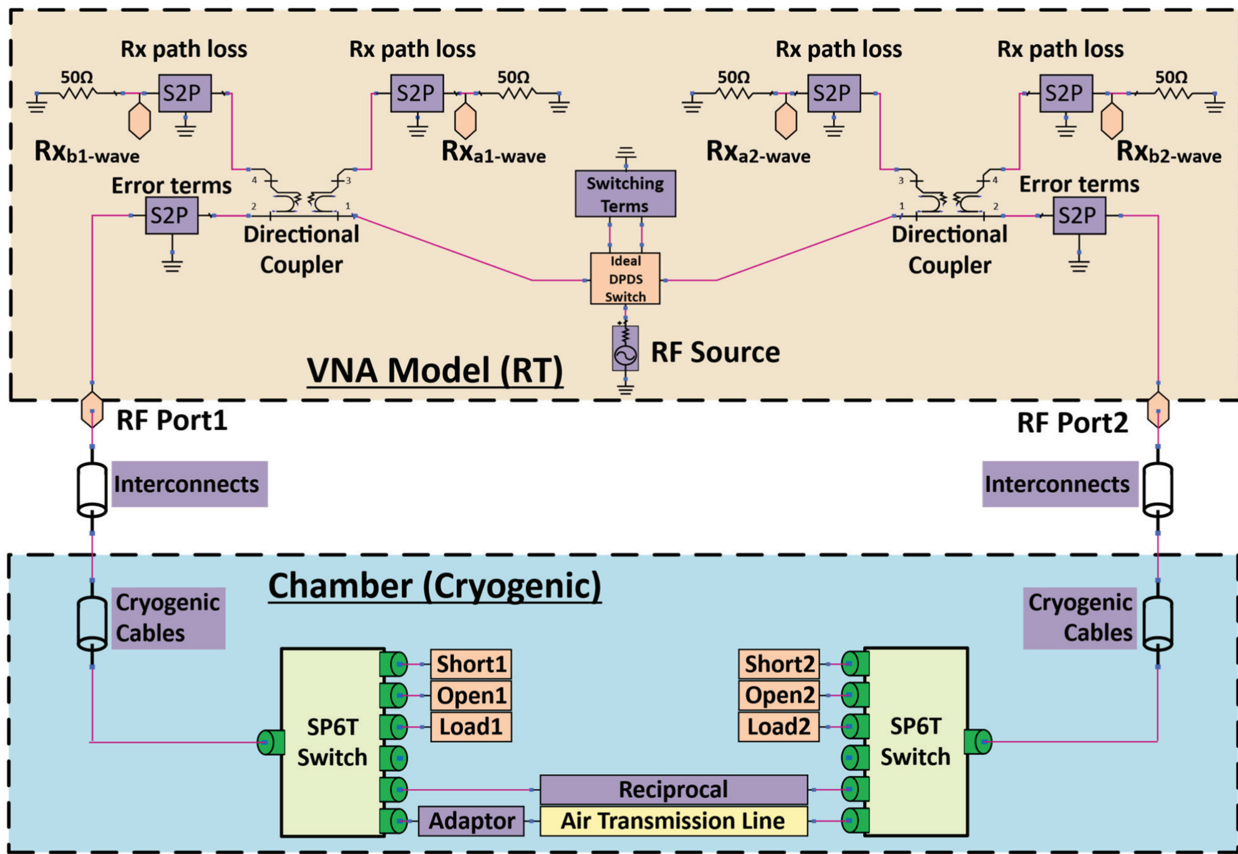

Fig. 8. Simplified sketch representing the ADS schematic environment of the MM, including the various sub-blocks based on measurements for VNA model and test-setup components.

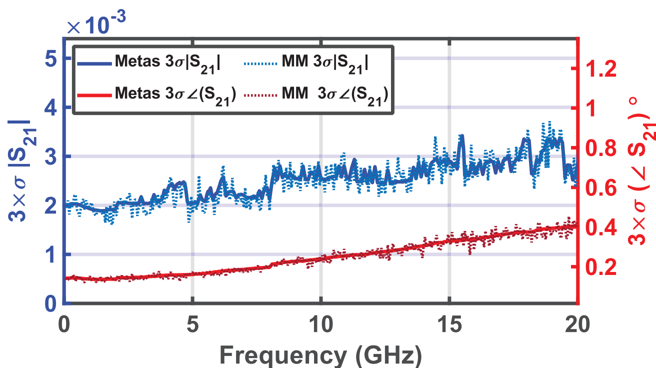

Fig. 9. RT comparison of uncertainty (3σ) prediction of MM versus Metas VNATools on Magnitude and phase of S_{21} of a Thru connection. Interconnects temperature gradient and fluctuations inclusion.

to the noise model presented in [42], based on multiplicative and additive noise contributions, modeling both the trace-noise and the noise floor of the VNA. The frequency-dependent coefficients to model these noise contributions are experimentally characterized by employing repeated measurements on high-reflective and transmissive devices [43]. The standard deviation of both magnitude and phase of the incident and reflected waves are acquired at low power levels, to quantify the additive component, and at increasing power levels to quantify the multiplicative component.

Fig. 9 shows the validation of the proposed ADS-based VNA model versus METAS VNAtools [40] in an RT experiment. The experimental setup consists of a VNA (measured for its noise contribution in both VNAtools and the proposed ADS MM) and a 3.5 mm calibration kit, measured at the VSL laboratories. A Monte Carlo analysis with 100 iterations is used in the MM to generate the uncertainty bound on a nonzero Thru connection, used as a DUT, of which the 3σ uncertainties of S_{21} magnitude and phase responses are shown in Fig. 9. The good agreement between the two tools provides confidence in the proposed VNA noise model implementation, which will be used for the cryogenic setups considered in this work.

V. Temperature Gradient and Fluctuation of Cables

As stated in Section IV, accurate evaluation of systematic errors is required for accurate assessment of the measurement uncertainty. Hence, in the cryogenic setups, it is important to include temperature gradients (systematic error) and temperature fluctuations (random error) effects over the different interconnections used across different stages of the cryostat.

To realize a versatile model of interconnects with a custom temperature gradient, CST simulations are used. By employing thermo-mechanical simulations on a short line section (i.e., 5 mm length) and computing the RF response over temperature using the EM simulator.

To enable Monte Carlo simulations for calculating uncertainties of a small temperature variation, i.e., $|\Delta T| \ll 1$ K,

Authorized licensed use limited to: TU Delft Library. Downloaded on December 08,2025 at 08:18:55 UTC from IEEE Xplore. Restrictions apply.

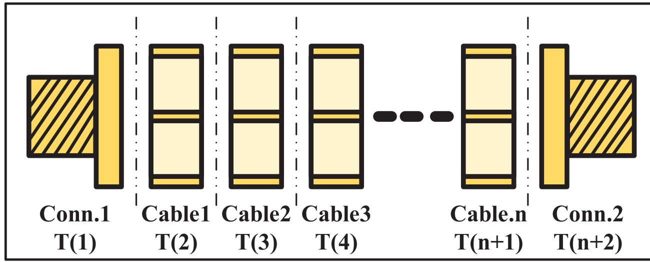

Fig. 10. Diagram of cascaded cable elements with different temperatures for the response of a cable with a temperature gradient.

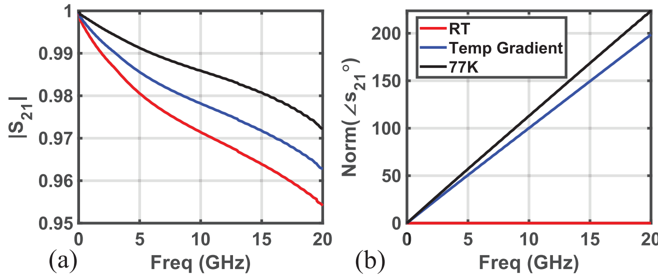

Fig. 11. Generated 60 cm cable S_{21} at three thermal conditions: RT, 77 K, and temp. Gradient from RT to 77 K (a) Magnitude and (b) phase normalized to RT case.

the response of each cable (sub)-section is computed by using linear interpolation on the magnitude and phase of the S-parameters over temperature.

The frequency and temperature (constant or gradient case) dependent cable with user-defined length is then computed by cascading the short cable sections. Each section is set at a uniform temperature and cascaded to realize the "complete" response of the cable, see Fig. 10.

To demonstrate the approach, in Fig. 11, we present the response of a 60 cm cable for three cases:

1) Constant RT temperature.
2) Linear gradient from RT to 77 K.
3) Constant 77 K temperature.

As can be seen in Fig. 11, the transmission loss and the phase delay of the cable follow the expected behavior with the temperature gradient case among other cases. The losses and phase delay reduce with temperature due to increased metal conductivity and shrinkage of the length of cables.

The proposed approach can then be employed to account for the temperature fluctuation effects on a cable experiencing a thermal gradient. In Fig. 12, the normalized thermal perturbations and the mean of $|S_{21}|$ and $\angle S_{21}$ is seen for a 60 cm cable, which has a linear temperature gradient from 300 K $\pm$ 0.5 K (rectangular distribution) at the start of the cable till the 15 cm point, from which it is at a constant 77 K (inside liquid nitrogen). In Section VIII, the effective uncertainty contribution of this effect in two different setups is reported.

VI. Switch Nonidealities

As mentioned, connectorized cryogenic setups commonly employ switches, as first demonstrated in [10], at the last cryostat stage, to allow calibration in a single cooling cycle. The

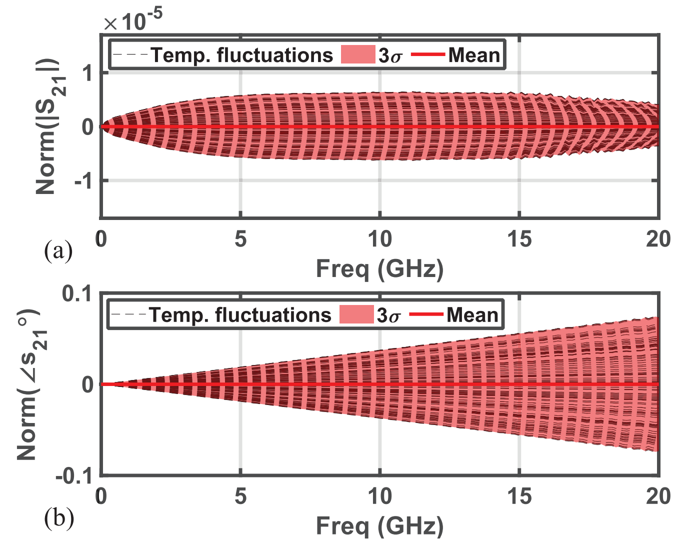

Fig. 12. Cable response with a temperature gradient of 300 K $\pm$ 0.5 K down to 77 K: Normalized $|S_{21}|$ and $\angle S_{21}$ response of equivalent cable with uncertainties versus individual cable responses affected by temperature fluctuations. (a) Norm $(|S_{ij}|) = |S_{ij}| - |\, S_{ij}$ Mean $|$. (b) Norm $(\angle S_{ij}) = \angle S_{ij} - \angle S_{ij}$ Mean.

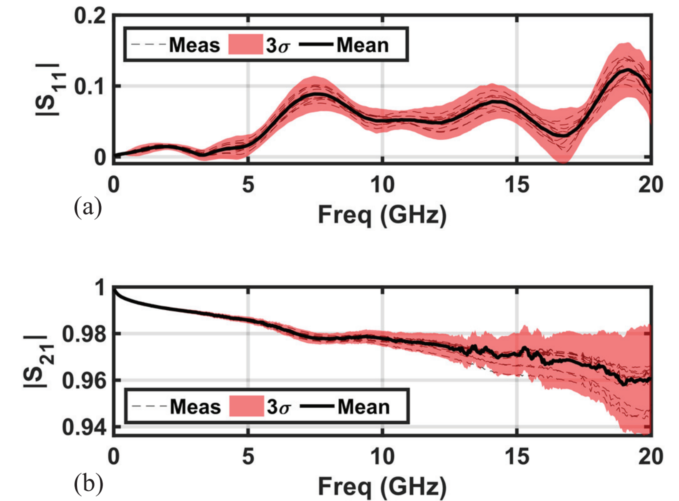

Fig. 13. Channel response (a) $|S_{11}|$ and (b) $|S_{21}|$ comparison among two switches at RT and the equivalent calculated uncertainty bound (3σ) used in this study (dashed lines).

downside of this approach is that it propagates the error arising from switch repeatability and switch asymmetries (among the different switch ports) on the calibrated DUT measurements. In this study, we characterize and use Radial SP6T SMA 26.5 GHz latching switches. The switches are first characterized for their repeatability, which is realized by performing 20 repeated reflection coefficient measurements of short-circuited switch channels. This test provided a repeatability error lower than 5E-3 at 20 GHz. Second, the 12 switch paths (six channels from two switches) are characterized independently, and their relative variation is plotted in Fig. 13, as a random uncertainty contribution, and is an order of magnitude larger than the repeatability effect.

The mean response of all switch channels from the RT characterization (shown in Fig. 13) was used in the MM as

Authorized licensed use limited to: TU Delft Library. Downloaded on December 08,2025 at 08:18:55 UTC from IEEE Xplore. Restrictions apply.

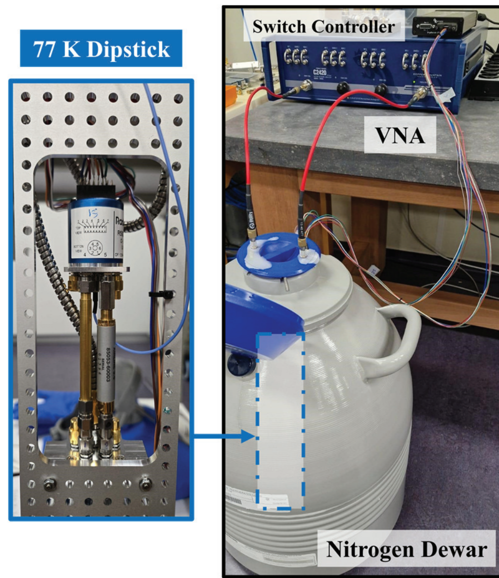

Fig. 14. 77 K dipstick with 75 mm air-lines and calibration standards installed on the switches (left) and the measurement setup including VNA and liquid nitrogen dewar (right).

an equivalent nondeterministic uncertainty in the Monte Carlo simulation.

VII. Cryogenic Measurement Validations

In this section, we report on the measurements performed on the coaxial air transmission line in the two cryogenic setups developed at VSL.

A. Measurement Setup for Model Validation at 77 K

For the validation at 77 K, a specific measurement setup was realized. It employs an RT VNA with connecting cables and a dipstick setup enabling full submergence in a liquid nitrogen dewar (see Fig. 14), the switches, calibration standards, and the DUT, a 75 mm precision coaxial air transmission line.

The fixture holding the switches allows the in-line (opposite face) positioning of the switches. Given that the chosen calibration algorithm, i.e., short, open, load, and reciprocal (SOLR), does not require any information on the reciprocal device, i.e., any uncharacterized cable can be employed, allows the distance between the two switches to be set by the DUT (i.e., coaxial air transmission line) without the need for auxiliary cables. This approach reduces the measurement uncertainty since further de-embedding of these auxiliary cables is no longer needed. As both switches have female ports, a male-male adaptor is used on one of the ports of the air transmission line and is then de-embedded using its RT measurement results.

The measurements were made using a 20 GHz four-port Copper Mountain VNA set at -10 dBm power level. In Fig. 15, the measurement results, including the uncertainties computed by the MM, are shown and compared with the results from the transmission line CST simulation (see Fig. 2).

Each plot shows two uncertainty bounds: a red one, representing (combined) measurement uncertainty calculated using the numerical MM, and a gray bound, representing uncertainties only from the calibration standards. In addition, the blue lines represent CST simulation results of the model of the transmission line.

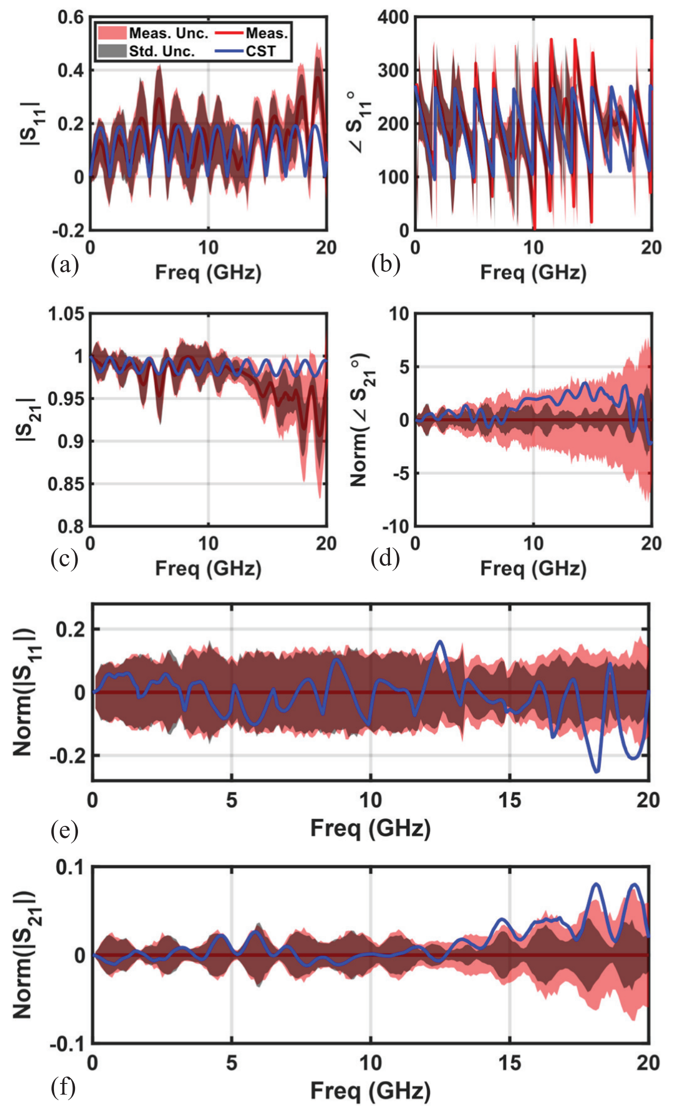

Fig. 15. Air transmission line parameters (a) $|S_{11}|$, (b) $\angle S_{11}$, (c) $|S_{21}|$, (d) Norm($\angle S_{21}$) at 77 K with MM uncertainties (3σ) versus CST model S-parameters red area shows the combined measurement uncertainty (Including the standards uncertainty) and gray area shows uncertainty caused only by standards, (e) Norm($|S_{11}|$), and (f) Norm($|S_{21}|$) of the air transmission line versus CST model. Norm($|S_{ij}|$) = $|S_{ij}| - |S_{ij}$ Meas|, Norm($\angle S_{ij}$) = $\angle S_{ij} - \angle S_{ij}$ Meas.

Given that the air transmission line is submerged in liquid nitrogen, in the 3-D model (see Fig. 2), air is replaced with the relative electrical permittivity of liquid nitrogen, i.e., ε_r = 1.45 [44]. As can be noticed by Fig. 15(a), the presence of nitrogen has shifted the response of the air transmission line from a highly matched component to a partially mismatched transmission line.

B. Measurement Setup for Model Validation at 4.2 K

For the measurements at 4.2 K, a similar setup was fabricated (shown in Fig. 16). It consists of the same VNA, connecting cables, and a dipstick designed for liquid helium

Authorized licensed use limited to: TU Delft Library. Downloaded on December 08,2025 at 08:18:55 UTC from IEEE Xplore. Restrictions apply.

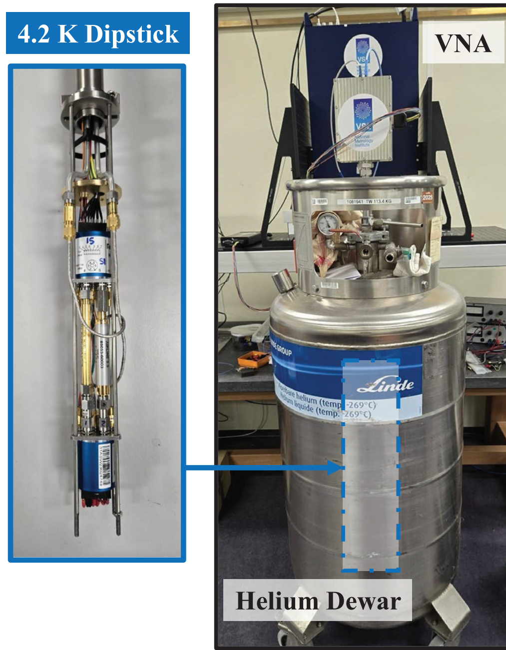

Fig. 16. 4.2 K dipstick with 75 mm air transmission lines and calibration standards installed on the switches (left) and the measurement setup including VNA and He dewar (right).

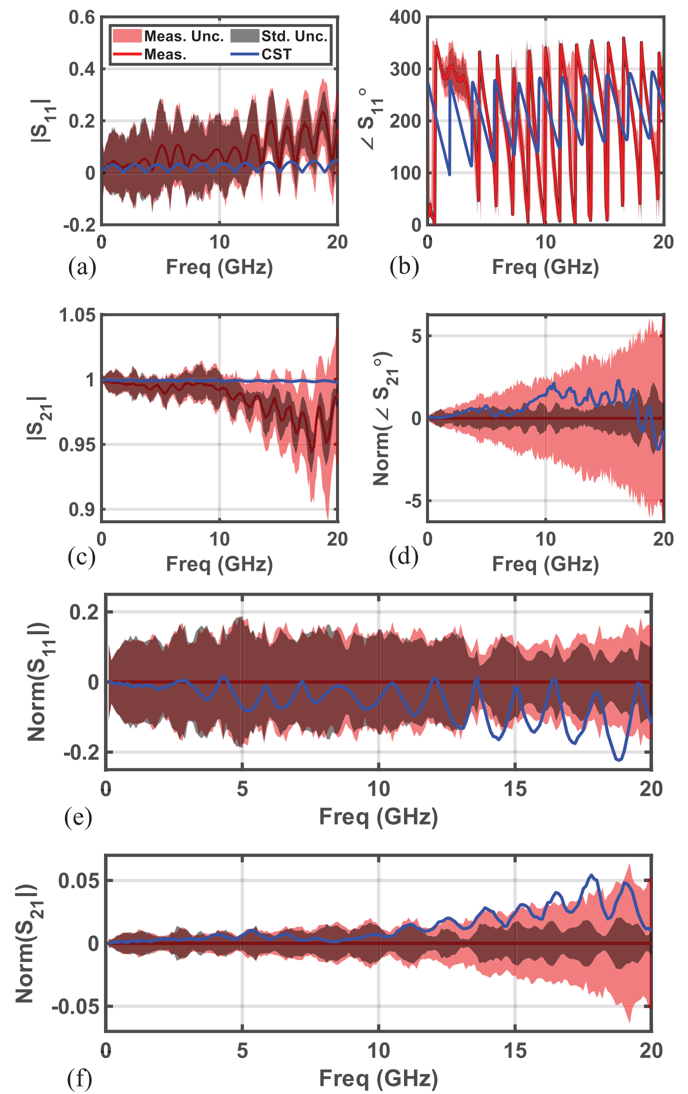

Fig. 17. Measurements of air transmission line at 4.2 K with MM uncertainties (3σ) versus CST model S-parameters. (a) $|S_{11}|$, (b) $\angle S_{11}$, (c) $|S_{21}|$, (d) Norm($\angle S_{21}$), (e) Norm($|S_{11}|$), and (f) Norm($|S_{21}|$).

wet measurements. Positioning the switches in the same configuration, facing each other, helps keep unnecessary uncertainties out of the experiment. Fig. 17 shows S-parameters of the coaxial air transmission line versus the CST model of the same line at 4.2 K (shown in Fig. 2). The airline simulation environment representing this setup has liquid He as the simulation background material replacing air. The relative permittivity of liquid helium (ε_r = 1.057 [45]) is much closer to that of air, hence the reflection coefficient of the line [Fig. 17(a)] is relatively smaller compared to the 77 K case.

VIII. Discussions

Figs. 15(a)–(f) and 17(a)–(f) provide a comparison of 77 K and 4.2 K measurement results with uncertainty bounds and thermo-mechanical EM model nominal and normalized curves. The general agreement between the experimental and modeling responses of the verification device confirms the validity of the proposed approach.

To explain the model exceeding the bounds in some frequency points, it is worth noting that the air transmission line model represents a best effort model of the actual device, mapping accurately its thermal, mechanical, and electrical properties. Nevertheless, it does not take into account uncertainties, and a small systematic offset is attributed to the following causes.

1) Transmission line manufacturing tolerances, including eccentricity of inner and outer conductors of the air transmission line [28].
2) Pin gap effect of connectors in coaxial measurements, as mentioned in [28] and [46].

In addition, the uncertainty bounds are partially underestimated due to the following procedure employed.

1) The switches' uncertainties contribution are based on their RT data.
2) The adaptor response used in the de-embedding process uses RT data.

Finally, the data shown in Table V does not include the drift effect of VNA and receiver linearity error, as with the measurements done in rapid succession after a long stabilization period in a temperature-controlled laboratory and sufficient power backoff from maximum VNA power, these contributions are not significant.

In Table V, the detailed contributions of each considered uncertainty source and its relative weight are summarized. As the numbers show, the switch asymmetries are a major contribution to the uncertainty budget at higher frequencies, further proving the claim by [10] and [14] and highlighting the need for methods to de-embed/mitigate these effects to significantly reduce the total uncertainty at these frequencies. The results also show that at the lower end of the spectrum, standard uncertainties are the most contributing factor. As the standard

Authorized licensed use limited to: TU Delft Library. Downloaded on December 08,2025 at 08:18:55 UTC from IEEE Xplore. Restrictions apply.

TABLE V

UNCERTAINTY CONTRIBUTORS FOR ALL THE SETUPS ON AIR TRANSMISSION LINE $|S_{21}|$ $\sigma = 3$ (RELATIVE PERCENTAGE)

77 K Setup			
	500 MHz	10 GHz	20 GHz
VNA Noise -10dBm/ 50Hz	7.11E-05 (0.001%)	1.19E-04 (0.005 %)	1.68E-04 (0.0012%)
Standard Uncertainty	0.0216 (99.52%)	0.015 (79.14%)	0.018 (13.79%)
Switch Asymmetry	0.0015 (0.48%)	0.0077 (20.85%)	0.045 (86.20%)
Temperature Fluctuations*	5.73E-06 (7E-6%)	5.91E-05 (1.2E-3%)	2.25E-04 (2.2E-3%)
Combined Uncertainty	0.0217	0.0169	0.0484
4.2 K Setup			
	500 MHz	10 GHz	20 GHz
VNA Noise -10dBm/ 50Hz	8.31E-05 (0.02%)	2.94E-04 (3.43%)	0.0021 (0.19%)
Standard Uncertainty	0.0063 (94.61%)	0.0138 (75.68%)	0.0096 (3.88%)
Switch Asymmetry	0.0015 (5.36%)	0.0072 (20.60%)	0.0477 (95.92%)
Temperature Fluctuations*	2.59E-5 (2E-3%)	8.36E-4 (0.28%)	1.95E-04 (1.6E-3%)
Combined Uncertainty	0.0065	0.0159	0.0487

*This item is calculated for a typical cable of the same length and material based on explanation of Fig. 12

uncertainties are mostly dependent on the load definition, this indicates that utilizing device-specific model tuning similar to [26] could potentially reduce the overall standard uncertainty contribution.

IX. CONCLUSION

In this contribution, we presented for the first time the usage of EM simulations to model broadband cryogenic calibration devices and to utilize perturbations in the model based on fabrication tolerances to calculate uncertainty bounds at user-defined cryogenic temperatures by leveraging thermo-mechanical simulations.

Furthermore, it was shown that using an MM for cryogenic setups, we could allow propagating uncertainties through systematic errors and calibration to device level, enabling the calculation of a complete uncertainty budget including cryogenic standard definition uncertainties, VNA noise, switch asymmetries, and temperature fluctuation effects on the cables/interconnects. In the end, the results were reported on measurements of the verification device, a coaxial air transmission line, in two setups operating at 77 K and 4.2 K, and compared the results with the EM model. In addition, a complete analysis of the uncertainty sources, including relative contributions, was attained using the MM, providing the capability to isolate the major uncertainty contributors in each frequency region.

Thanks to the isolated characterization approach of different uncertainty blocks (i.e., switches, VNA, and standards) proposed in this study, the methods described remain general and can be applied to different setup configurations at various temperatures.

ACKNOWLEDGMENT

The authors would like to thank John Martens (Anritsu Company) for providing the air transmission line mechanical schematics and James Kroll (TNO) for the constructive discussions.

REFERENCES

[1] J. Anders et al., "CMOS integrated circuits for the quantum information sciences," *IEEE Trans. Quantum Eng.*, vol. 4, pp. 1–30, Jul. 2023, doi: 10.1109/TQE.2023.3290593.

[2] J. E. Martin, N. P. Fox, and P. J. Key, "A cryogenic radiometer for absolute radiometric measurements," *Metrologia*, vol. 21, no. 3, pp. 147–155, Jan. 1985, doi: 10.1088/0026-1394/21/3/007.

[3] K. D. Irwin, "An application of electrothermal feedback for high resolution cryogenic particle detection," *Appl. Phys. Lett.*, vol. 66, no. 15, pp. 1998–2000, Apr. 1995, doi: 10.1063/1.113674.

[4] A. Steane, "Quantum computing," *Rep. Prog. Phys.*, vol. 61, no. 2, pp. 117–173, Feb. 1998, doi: 10.1088/0034-4885/61/2/002.

[5] J. Laskar, J. J. Bautista, M. Nishimoto, M. Hamai, and R. Lai, "Development of accurate on-wafer, cryogenic characterization techniques," *IEEE Trans. Microw. Theory Techn.*, vol. 44, no. 7, pp. 1178–1183, Jul. 1996, doi: 10.1109/22.508659.

[6] M. Goryachev, S. Galliou, and P. Abbé, "Cryogenic transistor measurement and modeling for engineering applications," *Cryogenics*, vol. 50, nos. 6–7, pp. 381–389, Jun. 2010, doi: 10.1016/j.cryogenics.2010.02.002.

[7] W. Chakraborty et al., "Characterization and modeling of 22 nm FDSOI cryogenic RF CMOS," *IEEE J. Explor. Solid-State Comput. Devices Circuits*, vol. 7, no. 2, pp. 184–192, Dec. 2021, doi: 10.1109/JXCDC.2021.3131144.

[8] B. Patra, M. Mehrpoo, A. Ruffino, F. Sebastiano, E. Charbon, and M. Babaie, "Characterization and analysis of on-chip microwave passive components at cryogenic temperatures," *IEEE J. Electron Devices Soc.*, vol. 8, pp. 448–456, 2020, doi: 10.1109/JEDS.2020.2986722.

[9] D. Kent Rytting, "Network analyzer accuracy overview," in *Proc. 58th ARFTG Conf. Dig.*, Nov. 2001, pp. 1–13, doi: 10.1109/ARFTG.2001.327486.

[10] L. Ranzani, L. Spietz, Z. Popovic, and J. Aumentado, "Two-port microwave calibration at millikelvin temperatures," *Rev. Sci. Instrum.*, vol. 84, no. 3, Mar. 2013, Art. no. 034704, doi: 10.1063/1.4794910.

[11] M. Stanley, S. De Graaf, T. Hönigl-Decrinis, T. Lindström, and N. M. Ridler, "Characterizing scattering parameters of superconducting quantum integrated circuits at milli-Kelvin temperatures," *IEEE Access*, vol. 10, pp. 43376–43386, 2022, doi: 10.1109/ACCESS.2022.3169787.

[12] M. Stanley et al., "Characterizing S-parameters of microwave coaxial devices with up to four ports at temperatures of 3 k and above for quantum computing applications," *IEEE Trans. Instrum. Meas.*, vol. 73, pp. 1–6, 2024, doi: 10.1109/TIM.2024.3369144.

[13] S. Simbierowicz, V. Y. Monarkha, S. Singh, N. Messaoudi, P. Krantz, and R. E. Lake, "Microwave calibration of qubit drive line components at millikelvin temperatures," *Appl. Phys. Lett.*, vol. 120, no. 5, Jan. 2022, Art. no. 054004, doi: 10.1063/5.0081861.

[14] M. Stanley, S.-H. Shin, J. Skinner, J. Urbonas, and N. Ridler, "Characterising scattering parameters of coaxial microwave devices at milli-kelvin temperatures for quantum computing technologies," in *Proc. 53rd Eur. Microw. Conf. (EuMC)*, Sep. 2023, pp. 150–153, doi: 10.23919/EuMC58039.2023.10290560.

[15] T. Arakawa and S. Kon, "Calibrated two-port microwave measurement up to 26.5 GHz for wide temperature range from 4 to 300 k," *IEEE Trans. Instrum. Meas.*, vol. 72, pp. 1–8, 2023, doi: 10.1109/TIM.2023.3315393.

[16] S.-H. Shin, M. Stanley, J. Skinner, S. E. de Graaf, and N. M. Ridler, "Broadband coaxial S-parameter measurements for cryogenic quantum technologies," *IEEE Trans. Microw. Theory Techn.*, vol. 72, no. 4, pp. 2193–2201, Apr. 2024, doi: 10.1109/TMTT.2023.3322909.

Authorized licensed use limited to: TU Delft Library. Downloaded on December 08,2025 at 08:18:55 UTC from IEEE Xplore. Restrictions apply.

[17] H. Wang et al., “Cryogenic single-port calibration for superconducting microwave resonator measurements,” *Quantum Sci. Technol.*, vol. 6, no. 3, Jul. 2021, Art. no. 035015, doi: 10.1088/2058-9565/ac070e.

[18] A. Ferrero and U. Pisani, “Two-port network analyzer calibration using an unknown ‘thru,”’ *IEEE Microw. Guided Wave Lett.*, vol. 2, no. 12, pp. 505–507, Dec. 1992, doi: 10.1109/75.173410.

[19] X. Xue et al., “CMOS-based cryogenic control of silicon quantum circuits,” *Nature*, vol. 593, no. 7858, pp. 205–210, May 2021, doi: 10.1038/s41586-021-03469-4.

[20] IS, C. I. and A. MAYNOTBE, *Guide to the Expression of Uncertainty in Measurement—Part 6: Developing and Using Measurement Models*, Joint Committee Guides Metrol. (JCGM), Sevres, France, Jan. 2020, doi: 10.59161/JCGMGUM-6-2020.

[21] *RF Termination—Coaxial≫ 2021-5001C-CRYO*. Accessed: Mar. 22, 2025. [Online]. Available: https://www.rfmw.com/products/detail/20215001ccryo-xma/717879/?pid=

[22] *RF Termination—Coaxial≫ 2021-5002C-CRYO*. Accessed: Mar. 22, 2025. [Online]. Available: https://www.rfmw.com/products/detail/20215002ccryo-xma/717880/?pid=

[23] *XMA Terminations // Item #2001-7010-0X*. Accessed: Mar. 22, 2025. [Online]. Available: https://www.xmacorp.com/product/2001-7010-0x/

[24] Microwave Studio(MWS). (2022). *CST-Computer Simulation Technology AG*. [Online]. Available: https://www.cst.com/products/cstmws

[25] D. M. Pozar, *Microwave Engineering*. Hoboken, NJ, USA: Wiley, 2012, p. 189.

[26] E. Shokrolahzade, F. Sebastiano, F. Mubarak, M. Babaie, and M. Spirito, “Impedance standard substrate characterization and EM model definition for cryogenic and quantum-computing applications,” in *IEEE MTT-S Int. Microw. Symp. Dig.*, Jun. 2023, pp. 557–560, doi: 10.1109/IMS37964.2023.10188097.

[27] L. Oberto et al., “Measurement and calibration approaches for two-port scattering parameters at mK temperatures,” in *Proc. Conf. Precis. Electromagn. Meas. (CPEM)*, Jul. 2024, pp. 1–2, doi: 10.1109/cpem61406.2024.10646000.

[28] U. Stumper, “Influence of nonideal calibration items on S-parameter uncertainties applying the SOLR calibration method,” *IEEE Trans. Instrum. Meas.*, vol. 58, no. 4, pp. 1158–1163, Apr. 2009, doi: 10.1109/TIM.2008.2006962.

[29] M. Garelli and A. Ferrero, “A unified theory for *S*-parameter uncertainty evaluation,” *IEEE Trans. Microw. Theory Techn.*, vol. 60, no. 12, pp. 3844–3855, Dec. 2012, doi: 10.1109/TMTT.2012.2221733.

[30] F. A. Mubarak, V. Mascolo, F. Hussain, and G. Rietveld, “Calculating *S*-parameters and uncertainties of coaxial air-dielectric transmission lines,” *IEEE Trans. Instrum. Meas.*, vol. 73, pp. 1–11, 2024, doi: 10.1109/TIM.2023.3338667.

[31] Bipm, Iec, I. ILAC, and I. Iupap, *Evaluation of Measurement Data—Supplement 1 to the ‘Guide to the Expression of Uncertainty in Measurement’—Propagation of Distributions Using a Monte Carlo Method*, Parc de Saint-Cloud, 2008.

[32] N. Simon, E. Drexler, and R. Reed, “Properties of copper and copper alloys at cryogenic temperatures,” Nat. Inst. Standards Technol. (NIST), Gaithersburg, MD, USA, Final Rep. NIST/MONO-177, Feb. 1992, doi: 10.2172/5340308.

[33] J. J. Corruccini and R. J. Gniewek, *Thermal Expansion of Technical Solids at Low Temperatures: A Compilation From the Literature*, U.S. Department of Commerce, National Bureau of Standards, Gaithersburg, MD, USA, 1961.

[34] M. V. Jacob, J. Mazierska, K. Leong, and J. Krupka, “Microwave properties of low-loss polymers at cryogenic temperatures,” *IEEE Trans. Microw. Theory Techn.*, vol. 50, no. 2, pp. 474–480, Feb. 2002, doi: 10.1109/22.982226.

[35] N. Simon, “Cryogenic properties of inorganic insulation materials for ITER magnets: A review,” Nat. Inst. Standards Technol., Boulder, CO, USA, Tech. Rep. NISTIR5030, 1994.

[36] *Mathworks, MATLAB*. Accessed: Mar. 22, 2025. [Online]. Available: https://www.mathworks.com/products/MATLAB.html

[37] J. Skinner, M. Stanley, J. Urbonas, S. de Graaf, T. Lindström, and N. Ridler, “Characterizing precision coaxial air lines as reference standards for cryogenic S-parameter measurements at milli-Kelvin temperatures,” in *IEEE MTT-S Int. Microw. Symp. Dig.*, Dec. 2023, pp. 561–564, doi: 10.1109/IMS37964.2023.10188171.

[38] D. F. Williams and R. B. Marks, “Calibrating on-wafer probes to the probe tips,” in *Proc. 40th ARFTG Conf. Dig.*, Dec. 1992, pp. 136–143, doi: 10.1109/arftg.1992.327008.

[39] *Keysight Advance Design System (ADS)*. Accessed: Mar. 22, 2025. [Online]. Available: https://www.keysight.com/us/en/products/software/pathwave-design-software/pathwave-advanced-design-system.html

[40] M. Wollensack, J. Hoffmann, J. Ruefenacht, and M. Zeier, “VNA Tools II: S-parameter uncertainty calculation,” in *Proc. 79th ARFTG Microw. Meas. Conf.*, Jun. 2012, pp. 1–28, doi: 10.1109/ARFTG79.2012.6291183.

[41] A. Lewandowski, D. F. Williams, P. D. Hale, J. C. M. Wang, and A. Dienstfrey, “Covariance-based vector-network-analyzer uncertainty analysis for time{-} and frequency-domain measurements,” *IEEE Trans. Microw. Theory Techn.*, vol. 58, no. 7, pp. 1877–1886, Jul. 2010.

[42] F. A. Mubarak, R. Romano, L. Galatro, V. Mascolo, G. Rietveld, and M. Spirito, “Noise behavior and implementation of interferometer-based broadband VNA,” *IEEE Trans. Microw. Theory Techn.*, vol. 67, no. 1, pp. 249–260, Jan. 2019, doi: 10.1109/TMTT.2018.2874667.

[43] (2000). *EA Guidelines on the Evaluation of Vector Network Analysers (VNA)*. [Online]. Available: https://www.papers3://publication/uuid/57D7D1B5-5D06-44A2-B13C-0AFF5D482B34

[44] J. E. Jensen, R. G. Stewart, W. A. Tuttle, and H. Brechna, “*Brookhaven National laboratory selected cryogenic data notebook: Sections I-IX*, vol. 1, ” U.S. Atomi. U.S. At. Energy Commission: Brookhaven Nat. Lab., Upton, NY, USA, 1980.

[45] W. Hartung et al., “RF performance of a superconducting S-band cavity filled with liquid helium,” in *Proc. 23rd Int. Linear Accel. Conf. (LINAC)*, 2006, pp. 755–757.

[46] J. P. Hoffmann, P. Leuchtmann, and R. Vahldieck, “Pin gap investigations for the 1.85 mm coaxial connector,” in *Proc. Eur. Microw. Conf.*, Oct. 2007, pp. 388–391, doi: 10.1109/EUMC.2007.4405208.

Authorized licensed use limited to: TU Delft Library. Downloaded on December 08,2025 at 08:18:55 UTC from IEEE Xplore. Restrictions apply.